

Contents lists available at ScienceDirect

# Corrosion Science

journal homepage: www.elsevier.com



# Corrosion and tribocorrosion mitigation of perhydropolysilazane-derived coatings on low carbon steel

Ni Yang , Wenbo Wang , Wenjun Cai , Kathy Lu  $_{st}$ 

Department of Materials Science and Engineering, Virginia Polytechnic Institute and State University, Blacksburg, VA 24061, USA

# ARTICLE INFO

# Keywords: Perhydropolysilazane Silicon oxynitride Steel Corrosion Tribocorrosion

#### ABSTRACT

Perhydropolysilazane (PHPS) is a polymer with [-SiH<sub>2</sub>-NH-]<sub>n</sub> repeating units. By pyrolysis with PHPS as a precursor, highly adhesive and protective silicon oxynitride (SiON)-based coatings were synthesized. The formation of Si—O—Si bonds increased with pyrolysis temperature. Both the hardness and Young's modulus of the PHPS-derived coatings were enhanced at higher pyrolysis temperatures. The PHPS-derived coatings significantly enhanced the corrosion resistance of low carbon steel in a 0.6 M NaCl aqueous solution, especially for the coatings with the formation of extensive Si-O-Si bonds. The PHPS-derived coating at the pyrolysis temperature of 600 °C exhibited the best resistance to corrosion and tribocorrosion.

#### 1. Introduction

Low carbon steels (LCS), which have less than 0.20 wt% carbon content, are very likely to be oxidized into rust when being exposed to different corrosive conditions, such as air, moisture, or chemical components [1,2]. In order to expand their vast applications in multiple areas, such as automobiles [3], power plants [4], oilfields [5], and aircrafts [6], protective coatings are necessary. In recent years, metallic, polymeric, and ceramic-based coatings have been applied to the surface of LCS and made notable gains in their corrosion resistance [7-11]. For example, Ni-Cr alloy coatings were deposited on ST37 steel sheets from a Cr (III)-Ni (II) bath solution and the alloy coating containing 39.8 wt% Cr had the best corrosion resistance [12]. A polyaniline/polyvinyl chloride blended coating improved the anti-corrosion ability compared to bare 1010 steel after exposure to saline and acidic test media, achieving the highest charge transfer resistance values based on the EIS measurements [13]. An adherent poly(o-toluidine) was successfully synthesized on LCS, and the corrosion potential was ~334 mV more positive for poly(o-toluidine)-coated LCS than that of bare LCS in a 3% NaCl aqueous solution [14]. However, a metallic coating has an adverse environmental impact because of the toxicity from heavy metals. Also, galvanic corrosion may occur when two different metallic materials are electrically coupled in a conductive environment [15]. As for polymeric coatings, the coating formation processes are complicated and expensive. Pinholes can appear on

the surface from wear and tear, which can lead to further corrosion [16]. In the long run, ceramic-based coatings have more advantages over metallic and polymeric ones, especially in light of their excellent wear and corrosion resistances.

Silicon-based oxide coatings (SiO2, SiOC, SiON, SiBONC, etc.) attracted widespread attention for improving corrosion and degradation resistance against high-temperature oxidation of metals [17-20]. They provided excellent thermal stability, high-temperature strength, and creep resistance [17,21,22]. A number of techniques have been used to prepare silicon-based coatings, such as physical vapor deposition (PVD) [23], chemical vapor decomposition (CVD) [24], sol-gel [25], vacuum arc deposition [26], and plasma-spraying [27]. However, these coating formation methods were expensive and complex. Also, the studies mainly focused on metal degradation in high-temperature gaseous environments, especially for water vapor-containing conditions [28,29]. The PHPS coatings pyrolyzed at 800 °C showed excellent high-temperature oxidation protection in  $Ar + H_2O$ ,  $Ar + O_2$ , and  $Ar + CO_2$ , where SiON was the main contributor to the oxidation resistance [29]. There have been few studies on corrosion prevention from such coatings at room temperature in aqueous systems.

A relatively low-cost and simple method is polymer-derived ceramics (PDCs) by pyrolysis of preceramic polymers. Compared to the above-mentioned preparation methods, the composition, microstructure, and thus performance of PDCs can be widely tuned depending on the polymer precursors and the pyrolysis conditions [30]. The materials prepared by the PDC route can offer enhanced physical/chemi-

Corresponding author.
 Email address: klu@vt.edu (K. Lu)

Table 1
Sample preparation parameters.

Group	Sample ID	Pre-pyrolysis Treatment	Pyrolysis Temperature	
1	PHPS/LCS-RT	NA	NA	
2	PHPS/LCS-200°C	100°C, 12 h	200°C	
3	PHPS/LCS-600°C	100°C, 12 h	600°C	

 Table 2

 Summary of the tribocorrosion testing parameters.

Conditions	Countanhadu	Took home	Load	Sliding velocity	Potential (V vs. Ag/
Conditions	Counterbody	Test type	(N)	(mm/s)	AgCl)
(1)	Al <sub>2</sub> O <sub>3</sub> (4 mm diameter)	Reciprocating	1	0.1	Start -0.1 V vs. OCP and finish 1 V vs. OCP at 1 mV/s scan rate
(2)	Al <sub>2</sub> O <sub>3</sub> (4 mm diameter)	Reciprocating	1	0.1	Under OCP
(3)	Diamond tip (12.5 µm radius)	Single pass	0-0.2	0.05	0.4 V anodic potential above OCP

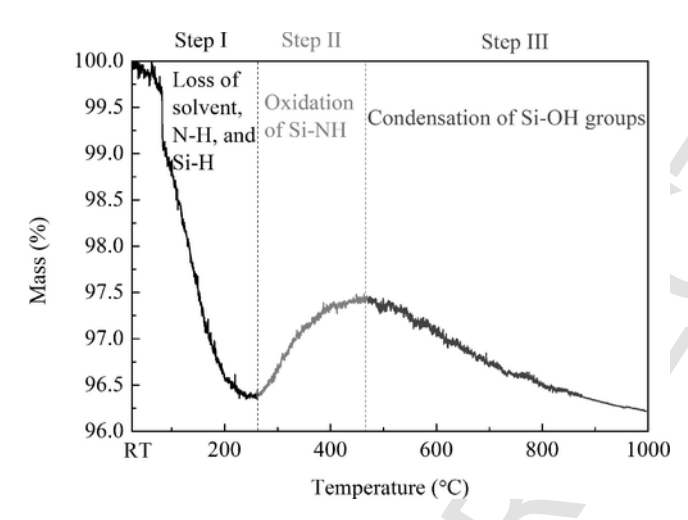


Fig. 1. Weight change as a function of pyrolysis temperature for the air-exposed PHPS as measured by TGA.

cal properties and possibly new attributes [31]. One of such polymer precursors is perhydropolysilazane (PHPS), which is composed of  $[-H_2Si-NH-]_n$  [32,33] and has the unique ability to convert to silicon oxynitride (SiON), Si<sub>3</sub>N<sub>4</sub>, or SiO<sub>2</sub> dense structures under different pyrolysis conditions [34,35]. A cross-linked PHPS coating on an aluminum 5086 substrate [36] showed about three orders of magnitude higher corrosion resistance and enabled a 1000 times longer lifespan. Thus, PHPS-derived coatings can be a great corrosion prevention solution for LCS. Although past research has been carried out on the conversion of PHPS to SiON coatings and the corresponding coating resistance against oxidation has been evaluated [23,34,37-39], few reported the electrochemical properties and tribocorrosion resistance of such coatings under water immersion conditions at room temperature. Understanding the structural evolution of different low temperature PHPS-derived coatings and their protection effectiveness for LCS corrosion in aqueous conditions is needed.

This work aims to synthesize different PHPS-derived coatings on LCS substrates and study their protection capability against corro-

sion and tribocorrosion in a 0.6 M NaCl aqueous solution. An economical method for applying PHPS-derived coatings on LCS is presented. Effects of pyrolysis temperatures on coating formation, coating-substrate adhesion, corrosion, and tribocorrosion are investigated.

#### 2. Materials and methods

#### 2.1. Materials preparation and synthesis

A cold rolled LCS sheet (A366/1008, 0.7595 mm thickness) containing 99.31–99.70 wt% Fe, 0.30 – 0.50 wt.% Mn, 0.04 wt.% P, and 0.05 wt.% S was cut into coupons of  $\sim\!1.7\times1.7\times0.7$  mm³ and mechanically polished with SiC papers (Allied High-Tech Products Inc, Compton, CA) from 320 to 1200 grit sizes, followed by polishing using diamond pastes (Allied High-Tech Products Inc, Compton, CA) from 6 to 0.5  $\mu$ m sizes. The uncoated and polished steel samples were cleaned in acetone by ultrasonic treatment and oven-dried at 80 °C for 30 s. A commercially available solution of 20 wt% PHPS in dibutyl ether was chosen as the coating precursor (PHPS NN 120-20, Clariant Advanced Materials GmbH, Sulzbach, Germany). Too high a concentration of PHPS makes it less stable and susceptible to oxidation. If the concentration of PHPS is too low, it is not easy to form a continuous film.

A spin coating method was applied on the polished samples at 1000 rpm for 50 s, with an acceleration rate of 150 rpm/s (Easy Coater 6, Schwan Technology, China). During the spinning, a single drop of the PHPS solution was put onto a rotating LCS sample. The spin-coated samples were divided into three groups and the details were shown in Table 1. Group 1 was left at room temperature, labeled as PHPS/LCS-RT, without any heat treatment for crosslinking. Groups 2 and 3 were both cross-linked in air and any pores from the evaporation of the solvent or gases [40] were eliminated. Afterwards, the pyrolysis was conducted in a muffle furnace (Thermo Scientific, Model No. F48015-60, Waltham, MA) in air at 200 °C and 600 °C using a heating and cooling rate of 25 °C / min<sup>-1</sup> with no holding time. After the pyrolysis, Groups 2 and 3 were marked as PHPS/LCS-200 °C and PHPS/LCS-600 °C, respectively.

# 2.2. Characterization

The thermal profile of the pure PHPS sample without LCS was obtained by thermogravimetric analysis using a Q50 TGA (TA Instruments, New Castle, DE) from room temperature to 1000°C at a heating rate of 10 °C/min and an air flux of 60 mL/min. The chemical bonds of the PHPS-derived coating without LCS were measured using Fourier Transform Infrared Spectroscopy (FTIR) (Thermo Scientific, Waltham, MA) between 500 and 2500  $\rm cm^{-1}$  wavenumber with a resolution of  $4\,\rm cm^{-1}$ and averaged between 128 scans. Two measurements were repeated on each sample to ensure reproducibility for TGA and FTIR analyses. The surface morphology and elemental distribution of the PHPS-derived coatings before and after corrosion/tribocorrosion tests were characterized using a field-emission scanning electron microscope (LEO 1550, Carl Zeiss MicroImaging, Inc. Thornwood, NY) equipped with an Energy Dispersive X-Ray Spectrometer (EDS, QUANTAX 400, Bruker AXS, Madison, WI). The cross-sections of the PHPS-derived coatings prior to and post the corrosion tests were measured by SEM on FIB (FEI Helios 600 Nano Lab, Hillsboro, OR).

The mechanical properties of the samples were evaluated by nanoindentation tests (Hysitron Ti900) using a standard Berkovich diamond indenter following the Oliver and Pharr method [41,42]. In this method, the slope of the unloading curve can be used to estimate the modulus of the coating systems based on the Oliver and Pharr equation [41,42]:

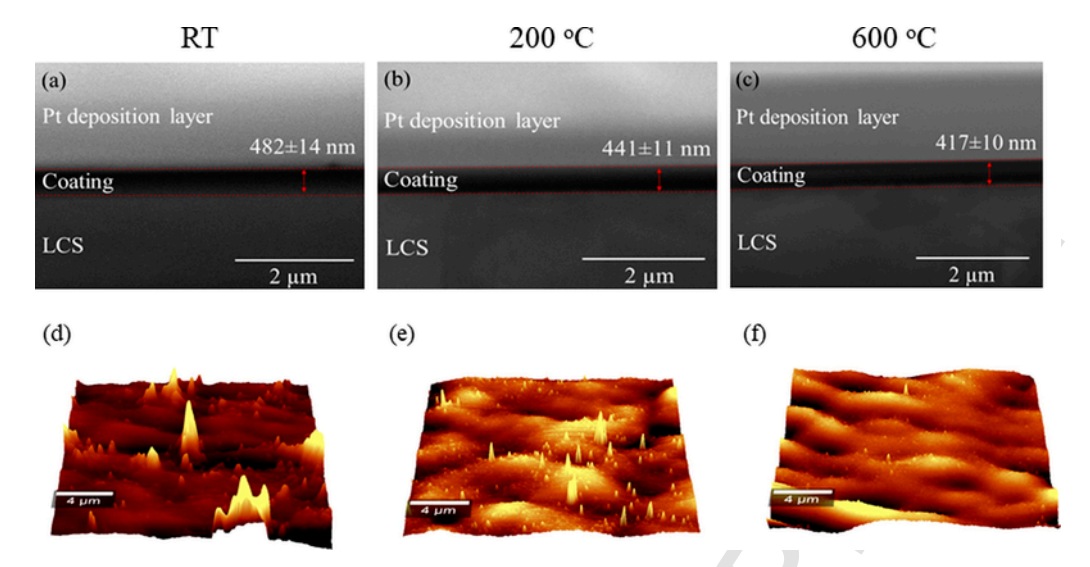


Fig. 2. (a-c) Cross-sectional SEM and (d-f) AFM surface images of the coating/LCS system at various pyrolysis temperature. (a) and (d) are for PHPS/LCS-RT sample, (b) and (e) are for PHPS/LCS-200 °C sample, while (c) and (f) are for PHPS/LCS-600 °C sample.

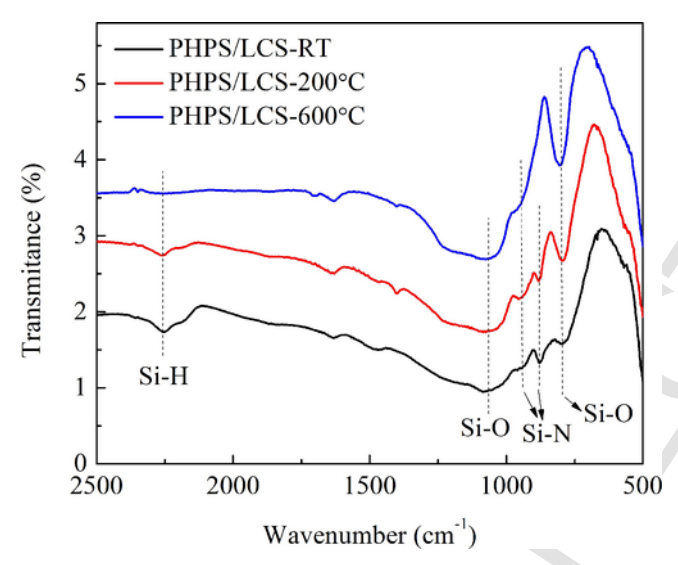


Fig. 3. FTIR spectra of the PHPS-derived coatings treated at different temperatures in air.

$$\frac{1}{E_{eff}} = \frac{(1 - \nu^2)}{E} + \frac{(1 - \nu_i^2)}{E_i}$$
 (1)

where Eeff is the effective Young's modulus, E and Ei are Young's moduli of the coating system and indenter, respectively.  $\nu$  and  $\nu$ i represent Poisson's ratios for the coating system and indenter, respectively. The tip-area function was calibrated using a fused quartz sample prior to indentation. In order to minimize the substrate effect, the penetration depth (~90 nm) was controlled at <20 % of the total coating thickness (~450 nm), followed by a trapezoidal loading function with 5s loading/unloading time and 2s holding time. At least 15 tests were repeated on each sample in order to obtain an average value and standard deviation. Atomic force microscopy (AFM) images were taken with an AFM/Confocal/Raman integrated spectrometer (alpha500R, WITec GmbH) using tapping mode tips under ambient conditions in the intermittent contact mode. The spectra were recorded in a 20  $\times$  20  $\mu$ m<sup>2</sup> region. A progressive dry scratch test was carried out in air in order to evaluate the adhesion strength between the coating and the substrate using a diamond tip with a 12.5 µm radius by a multifunctional tri-

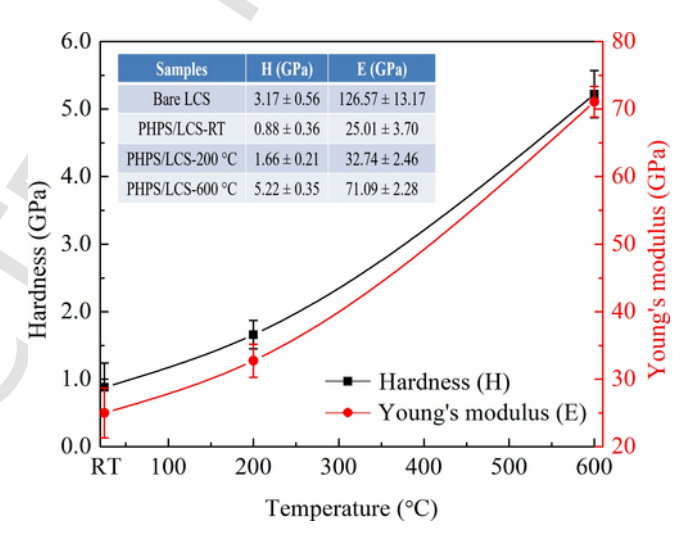


Fig. 4. Hardness (H) and Young's modulus (E) of the PHPS-derived coatings on LCS as a function of the pyrolysis temperature. The table insert shows the numerical values of H and E for all samples.

bometer (Rtec, CA, USA). Before the progressive scratch test starts, all samples had been immersed in a  $0.6\,\mathrm{M}$  NaCl solution for  $\sim\!15\,\mathrm{min}$  to reach a stable state. The sample surfaces were subjected to a progressive normal load from  $0\,\mathrm{N}$  to  $0.2\,\mathrm{N}$  over a  $3\,\mathrm{mm}$  stroke length and at a constant velocity of  $0.05\,\mathrm{mm/s}$ .

# 2.3. Corrosion and tribocorrosion tests

Potentiodynamic polarization (PD) and electrochemical impedance spectroscopy (EIS) tests were conducted in a naturally aerated 0.6 M NaCl aqueous solution (pH  $\sim\!6.4\pm0.3$ ) using a Gamry Reference 600® potentiostat (Warminster, PA, USA) to measure the corrosion behaviors of both uncoated and coated samples. At ambient temperature, a three-electrode configuration was used with the sample as the working electrode (WE), an activated titanium mesh as the counter electrode (CE), and a commercial silver-silver chloride electrode (1 M KCl internal solution) as the reference electrode (RE). An exposed area of  $\sim\!1\times1\,\mathrm{cm}^2$  was prepared on the samples using a protective stop-off lacquer. The PD tests were performed after 10 mins of stabilization at open circuit potential (OCP), at a constant rate of 1 mV/s, starting at a potential of  $\sim$  200 mV cathodic to OCP and terminated at  $\sim1.5\,\mathrm{V}$  over OCP.

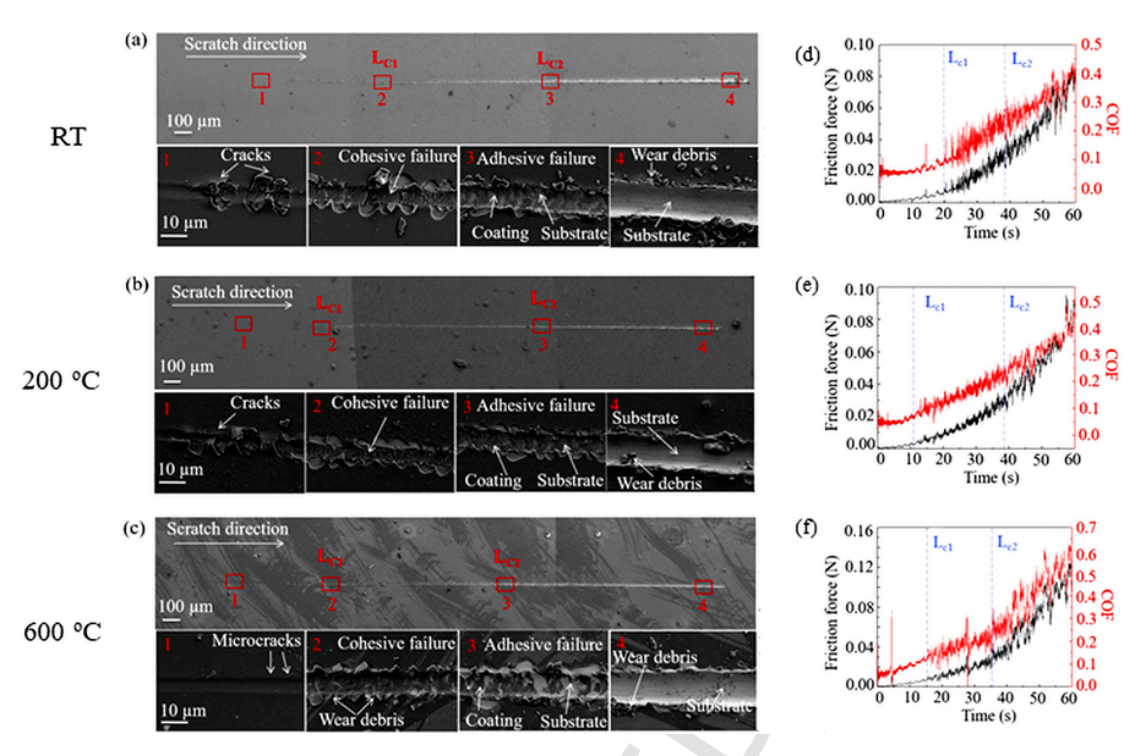


Fig. 5. (a-c) SEM micrographs of the scratch tracks and (d-f) the corresponding friction force and COF curves at different pyrolysis temperatures: (a, d) RT; (b, e) 200 °C; and (c, f) 600 °C.

Table 3
Critical loads and adhesion strength of the coated samples during the progressive dry scratch test.

Pyrolysis temperature	Lc <sub>1</sub> (N)	Lc <sub>2</sub> (N)	Adhesion strength (MPa)	Ż
RT	$0.075 \pm 0.03$	$0.124 \pm 0.02$	932.77 ± 8.20	
200 °C	$0.042 \pm 0.01$	$0.129 \pm 0.03$	$953.06 \pm 8.10$	
600°C	$0.057 \pm 0.02$	$0.115 \pm 0.01$	$895.49 \pm 4.21$	

All the EIS tests were carried out by applying an AC voltage of  $10\,\text{mV}$  rms in the 100 kHz-0.01 Hz frequency range (5 points per decade) at OCP with an equilibrium time of  $\sim\!300\,\text{s}$ . The obtained data were then fitted by a selected equivalent electrical circuit model using Gamry E-chem software (version 7.07). The tribocorrosion tests were performed in a 0.6 M NaCl aqueous solution at room temperature using a multifunctional tribometer (Rtec, CA, USA) connected with a three-electrode set-up, where the coated sample (with  $\sim\!\!1\times1.5\,\text{cm}^2$  ex-

posed area), an activated titanium mesh, and a 1 M KCl Ag/AgCl electrode were used as the working electrode, counter electrode, and reference electrode, respectively. Tribocorrosion tests were performed under the following three sets of conditions, as shown in Table 2, each with 60 s duration and 3 mm stroke length:

- (1) Constant load and ramping corrosion potential. The sliding test was conducted using a reciprocating-type alumina ball (Al $_2$ O $_3$ ,  $\Phi$  4 mm) on a plate with a 1 N constant load. The test was carried out at a scan rate of 1 mV/s, starting at a potential of  $\sim$  0.1 V vs.  $E_{ocp}$  and terminated at 1 V vs.  $E_{ocp}$ .
- (2) Constant load and open circuit potential (OCP). The same constant load and counter body as (1) were used while the samples moved in a linear-reciprocal motion under OCP.
- (3) Linear ramping load and constant anodic potential. A linear ramping load from 0N to 0.2N was applied and a diamond tip (12.5  $\mu m$  radius) was used as the probe to evaluate the protective effect of the coatings.

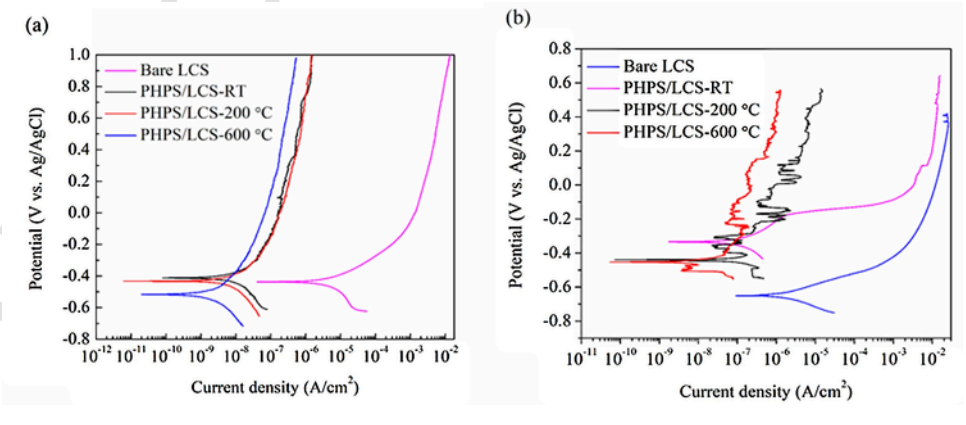


Fig. 6. Potentiodynamic polarization curves of the uncoated LCS and PHPS-coated LCS samples at (a) corrosion-only and (b) sliding conditions.

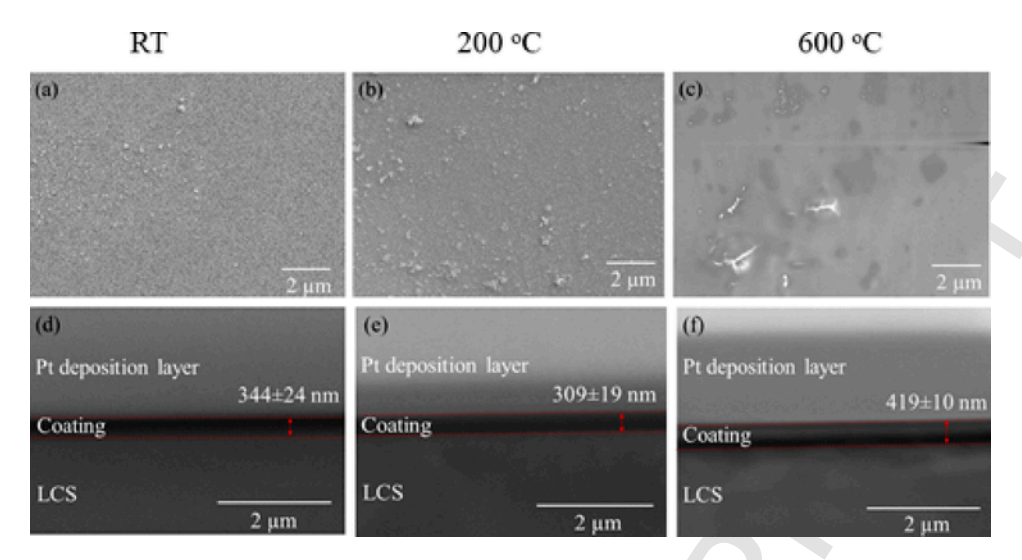


Fig. 7. SEM surface and cross-section images of the coating/LCS systems after corrosion test: (a, d) PHPS/LCS-RT, (b, e) PHPS/LCS-200 °C, and (c, f) PHPS/LCS-600 °C.

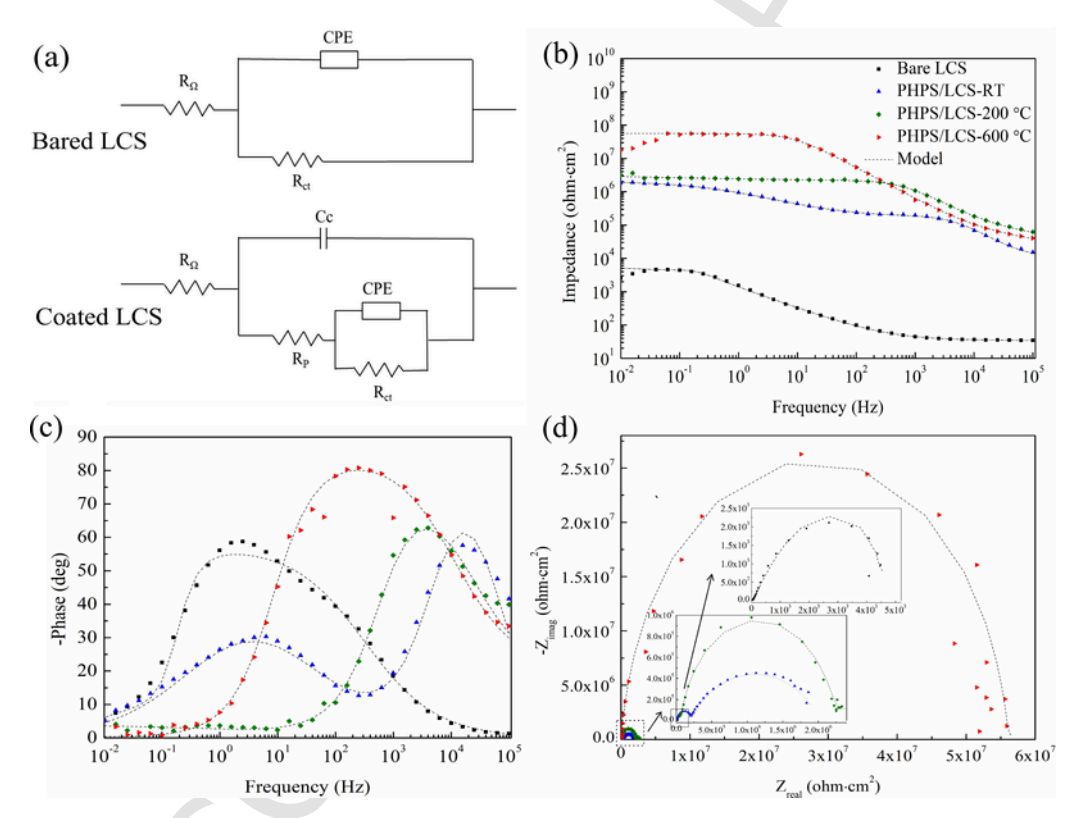


Fig. 8. (a) Equivalent electrical circuit, (b-c) Bode and (d) Nyquist diagrams obtained for bare LCS and PHPS coated LCS in the 0.6 M NaCl solution. Inset in (b) shows symbol legends for all data plotted in (b)-(d). Experimental results in (b-d) are fitted with model in (a) as dashed lines. Model fitting parameters are listed in Table 4.

 Table 4

 Summary of all fitting parameters for the equivalent circuit model in Fig. 8(a).

Sample	$R_{\Omega} (\Omega  cm^2)$	$R_p (\Omega  cm^2)$	$R_{ct}$ ( $\Omega$ cm <sup>2</sup> )	Cc (F cm <sup>-2</sup> )	Y (cm $^{-2}$ s $^{n}\Omega^{-1}$ )	n	CPE (F cm <sup>-2</sup> ·s <sup>n-1</sup> )
Bare LCS PHPS/LCS-RT PHPS/LCS-200°C PHPS/LCS-600°C	12.23 13.99 12.31 14.32	$\begin{aligned} & \text{NA} \\ & 1.01 \times 10^4 \\ & 2.26 \times 10^4 \\ & 4.78 \times 10^4 \end{aligned}$	$6.70 \times 10^{-2}$ $2.56 \times 10^{6}$ $3.78 \times 10^{6}$ $6.57 \times 10^{7}$	NA $6.65 \times 10^{-9}$ $6.06 \times 10^{-9}$ $4.95 \times 10^{-9}$	$6.29 \times 10^{-4}$ $2.25 \times 10^{-5}$ $1.77 \times 10^{-5}$ $1.40 \times 10^{-5}$	0.91 0.88 0.75 0.87	$\begin{array}{l} 4.45\times10^{-5} \\ 2.05\times10^{-5} \\ 1.64\times10^{-5} \\ 1.40\times10^{-5} \end{array}$

Prior to each type of the tribocorrosion tests, all the samples were immersed under OCP for  $\sim 15\,\mathrm{mins}$  to reach a stable state. After the tribocorrosion tests (1) and (2), the mass loss of the samples was ob-

tained using an analytical balance with a resolution of  $0.1\,\mathrm{mg}$ . Before and after measuring the mass loss, the specimen surfaces were cleaned ultrasonically with deionized water and dried in air. All the electrochemi-

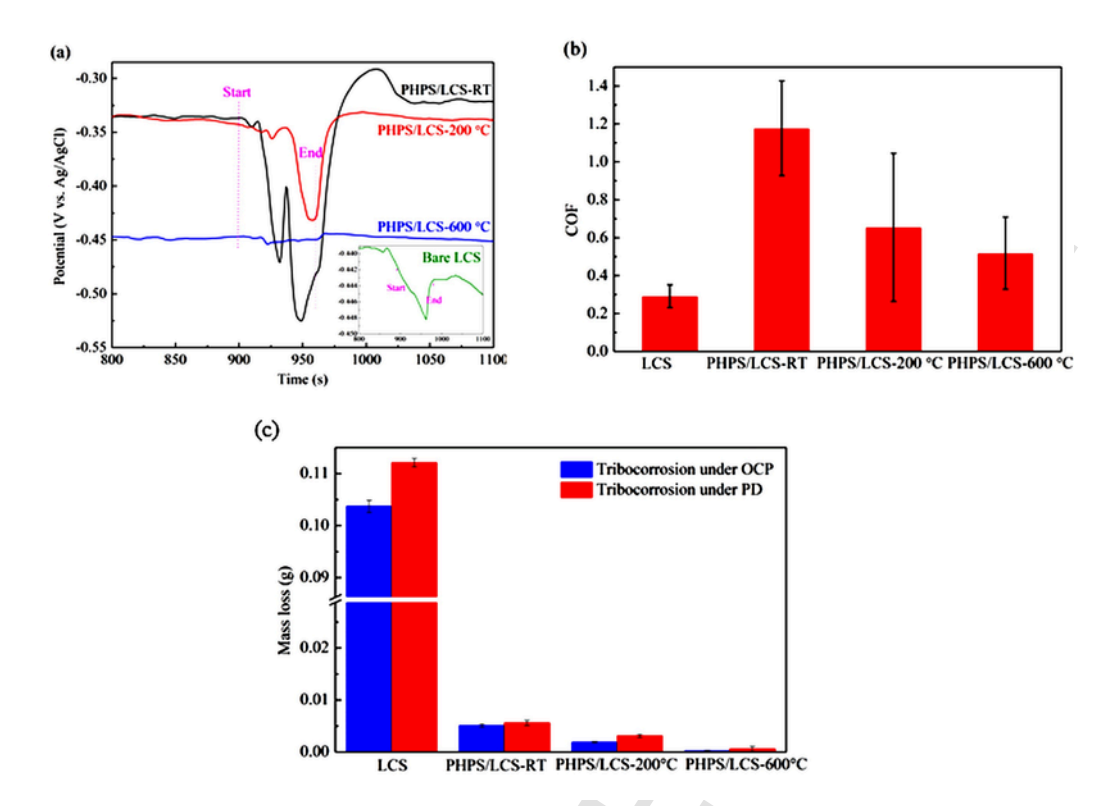


Fig. 9. (a) Evolution of corrosion potential before, during, and after tribocorrosion tests at open circuit potential in the 0.6 M NaCl solution, (b) values of COF after tribocorrosion and open circuit potential, and (c) mass loss of bare LCS and PHPS-derived coatings after tribocorrosion testing under open circuit potential and potentiodynamic polarization.

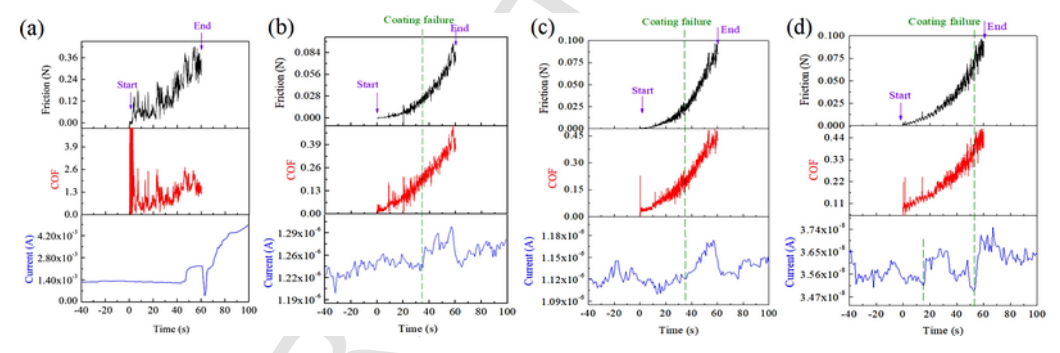


Fig. 10. Friction force, COF, and current of (a) bare LCS, (b) PHPS/LCS-RT, (c) PHPS/LCS-200 °C, and (d) PHPS/LCS-600 °C during the tribocorrosion tests. The negative value in the x-axis indicates the time before the progressive scratch test.

cal and tribocorrosion results reported were averaged from at least three repeated tests.

#### 3. Results and discussion

#### 3.1. Structural evolution

PHPS is very sensitive to air and reacts with atmospheric moisture (oxygen atom) to form Si—O bonds by hydrolysis of Si—H and Si—NH bonds [43]. Therefore, it is difficult to directly measure the thermal stability of liquid PHPS in an open-air condition. In this study, a gel-like PHPS was obtained by exposing the liquid PHPS to air at room temperature for 3h before conducting the TGA measurement. Fig. 1 indicates that the thermal evolution of PHPS in air contains three steps with a small weight loss (<4 wt%). During Step I, the PHPS displays a weight loss of 3.63 % between 90 °C and 250 °C, which can be attributed to the evaporation of the remaining organic solvent and the loss of N—H and Si—H species. It also demonstrates the importance of pre-heat treatment of the crosslinked coating before pyrolysis in or-

der to minimize the pore formation caused by the evaporation of the solvent. During Step II, a weight gain of  $\sim 1.06$  % is observed from 250–460 °C. Previous studies [34,44] suggest that such a quick weight gain before 510 °C is due to the oxidation of the Si-H bonds as well as the replacement of residual N atoms with O atoms according to:

$$\equiv$$
Si-NH + H<sub>2</sub>O  $\rightarrow$   $\equiv$ Si-OH +  $\equiv$ Si-NH<sub>2</sub> (2)

At  $\geq$ 460 °C, the weight loss should be mainly due to the condensation reaction of the Si–OH groups, as the silanol group has a strong tendency to undergo self-condensation process to produce compounds containing Si-O-Si bonds [45]:

$$\equiv$$
Si $-$ OH +  $\equiv$ Si $-$ NH<sub>2</sub>  $\rightarrow$   $\equiv$ Si $-$ O $-$ Si $\equiv$  + NH<sub>3</sub> $\uparrow$  (3)

Considering the small weight decrease at  $>600\,^{\circ}\text{C}$ , the changes in the coating thickness are expected to be minimal, as confirmed in Fig. 2

Fig. 2(a-c) display the SEM images of the cross-sectioned samples and the coatings are measured to be  $482 \pm 14 \,\text{nm}$ ,  $441 \pm 11 \,\text{nm}$ ,

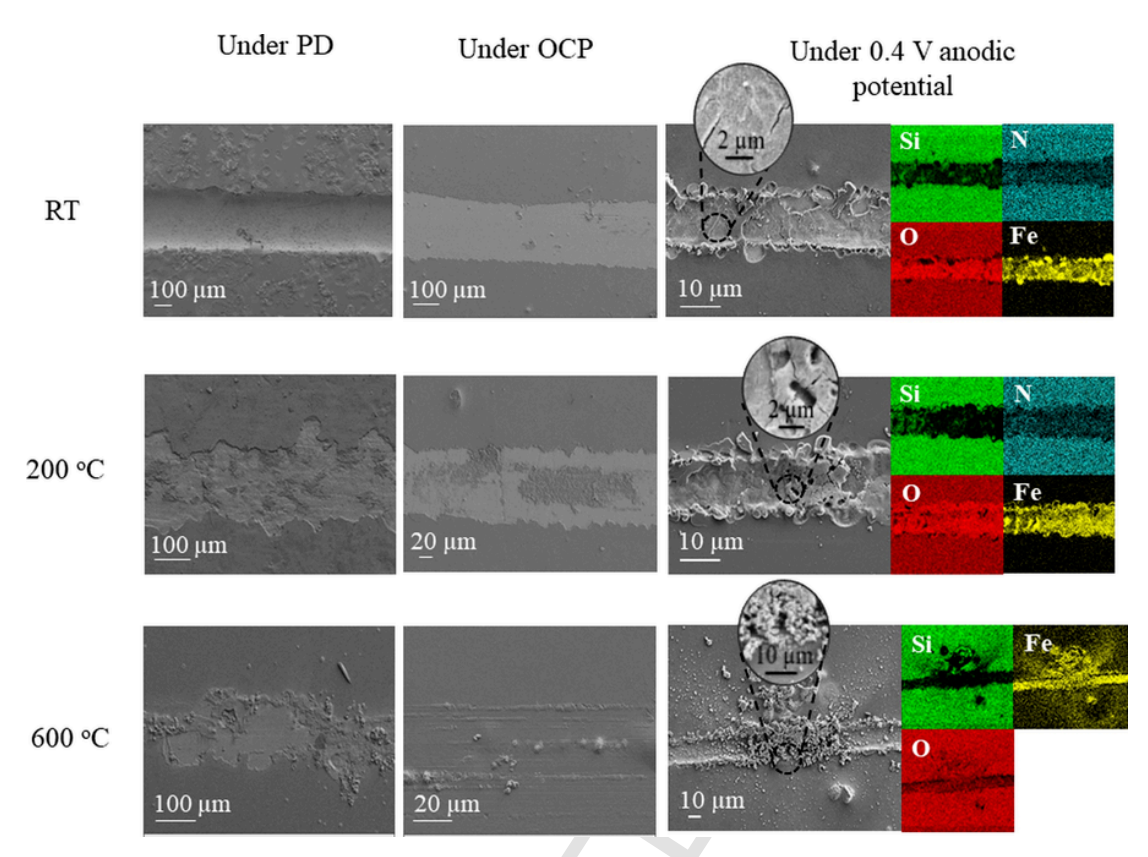


Fig. 11. SEM images of the wear tracks in the PHPS-derived coatings after tribocorrosion under different conditions. The color EDS maps correspond to the element distribution after tribocorrosion under 0.4V anodic potential.

and 417 ± 10 nm, respectively. A maximum thickness was achieved for the uncrosslinked sample at room temperature, due to the existence of dibutyl ether inside the coating, consistent with the TGA data (Fig. 1) that there is a continuous weight loss up to 3.63 %, attributing to the evaporation of the remaining organic solvent from 90 °C to 250 °C. This is also consistent with the thickness change from 482 nm to 441 nm from room temperature to 200 °C. The loss of the organic solvent results in a decrease in thickness. When the pyrolysis temperature increases to 600 °C, further thickness reduction from 441 nm to 417 nm is observed due to the condensation of the silanol groups (with loss of water). Overall, the change in the coating thickness is less than 13.5 % over the temperature range studied. Fig. 2(d-f) present the surface morphologies of the coatings. The average surface roughness decreases from  $44.88 \pm 0.18\,\text{nm}$  for the room temperature sample to  $23.25 \pm 1.82\,\text{nm}$ for the 600 °C treated sample, consistent with a previous study [46]. The surfaces of the PHPS-derived coatings become smoother with the pyrolysis temperature increase. As discussed, most of the dibutyl ether solvent can be evaporated from the uncured coating at 25-200 °C. When the crosslinked coating is treated at higher pyrolysis temperatures, the outmost layer of the coating becomes smooth and uniform due to the removal of the solvent and the crosslinking.

The structures of the coatings after different thermal processes are shown in Fig. 3, which provides a deeper understanding of the conversion behavior of the PHPS-derived coatings. The Si-H bonds located at  $\sim\!2250\,\mathrm{cm^{-1}}$  still exist for the PHPS/LCS-RT and PHPS/LCS-200 °C samples and indicate that the PHPS structure has not completely transformed into SiON yet in this temperature range. A higher pyrolysis temperature of 600 °C leads to the complete disappearance of the Si-H bonds. In terms of the Si-N bonds, the absorption band intensity dramatically decreases with the increase of the pyrolysis temperature but has not completely disappeared at 600 °C, consistent with a previous study [38]. N atoms are still present in the PHPS/LCS-600 °C sam-

ple. At the same time, the absorption bands from the Si-O bonds are located at 1102 and  $486~\rm cm^{-1}$  for all the samples. It means that the conversion from PHPS to Si-O-Si is activated even at room temperature, and a higher temperature enhances this process. The coatings do not transform completely into  $SiO_2$  under the chosen conditions, consistent with the literature [38]. Overall, the intensity of the Si—O bonds drastically increases while those for the Si—N and Si—H bonds decrease over the temperature range studied.

#### 3.2. Mechanical properties and coating adhesion

For the PHPS-derived coatings pyrolyzed at different temperatures, the hardness and Young's modulus are presented in Fig. 4. The hardness of the coatings increases with the pyrolysis temperature and is consistent with or higher than the literature values [47]. It is only  $\sim\!0.88\,\mbox{GPa}$  for the uncrosslinked coating and increases to  $\sim\!1.66\,\mbox{GPa}$  for the sample pyrolyzed at 200 °C with the removal of the organic solvent in the coating. With further temperature increase to 600 °C, the hardness of the PHPS-derived system increases even higher and reaches  $\sim\!5.22\,\mbox{GPa}$ . As more Si  $-\!\!\!\!-\!\!\!\!-\!\!\!\!\!-\!\!\!\!-\!\!\!\!\!$  Si bonds form during the high-temperature pyrolysis [44], as shown in Fig. 4, higher hardness values can be achieved.

The Young's moduli of the PHPS-derived coatings also show a similar trend, continually increasing as a function of the pyrolysis temperature. The Young's modulus for the uncrosslinked coating is only  $\sim\!25.01\,\mathrm{GPa}$  at room temperature. At 200 °C, the modulus reaches  $\sim\!32.74\,\mathrm{GPa}$ . At 600 °C, it exhibits higher modulus values of  $\sim\!71.09\,\mathrm{GPa}$ , due to the formation of SiON after the pyrolysis. Different from ionic bonds, covalent bonds are predominant for the SiON system, which has higher bonding strength and thus higher Young's modulus. Overall, the hardness and Young's modulus both increase with the pyrolysis temperature. Although broadly speaking there seems to be

a trend that hardness increases with Young's modulus, deviation has often been reported. In other words, a material with high hardness does not guarantee high Young's modulus, since the former involves plastic (bond breaking) and the latter involves elastic (bond stretching) deformation. For example, Choi et al. [48] recently synthesized a flexible (i.e., low Young's modulus) yet hard coating for foldable displays by highly cross-linked siloxane hybrids. This reported ceramic-based hybrid coating exhibits high strength like glass, yet high flexibility and elasticity. A coating with a higher hardness does not necessarily possess a higher Young's modulus at the same time.

A strongly adhesive PHPS-derived coating is desired for the surface protection of the LCS substrate. Previous research reported that the PHPS structure contains extensive Si-H groups and can easily react with –OH groups from a metal surface before a strongly adhesive coating forms [17,40,49–51]. A covalently bonded interface from the formation of metal—O—Si bonds is responsible for the strong adhesion according to:

$$Fe-OH + \equiv Si-NH-Si \equiv \rightarrow \equiv Fe-O-Si \equiv + H_2N-Si$$
(4)

$$Fe-OH + H_2N-Si = \rightarrow Fe-O-Si = + NH_3\uparrow$$
 (5)

Until now, little is known about the effect of the pyrolysis temperature on the coating adhesion. Since the destruction of the covalent bonds is at 410-650 °C [52], the coating adhesion could deteriorate in this pyrolysis temperature range. However, the enhancement of atomic interdiffusion across the coating-substrate interface promotes the adhesion strength [53]. To evaluate the coating-substrate adhesion, Fig. 5(a-c) show the changes in the friction force and coefficient of friction (COF) under a linear ramping load. Four specific locations have been selected to represent the gradual change of the scratch track with a transition from coating fragmentation at a low load to complete coating removal at a high load. At the low load stage, PHPS/LCS-RT and PHPS/ LCS-200°C have obvious cracks, while only microcracks are present along the edges of the scratch for PHPS/LCS-600°C, suggesting higher plastic deformation resistance from PHPS/LCS-600 °C. Afterwards, two critical loads, Lc1 (cohesive) and Lc2 (adhesive), are identified for each sample based on the surface morphology and load function, as summarized in Table 3. L<sub>c1</sub> is regarded as the load for cohesive failure with the start of coating chipping-up. L<sub>c2</sub> is considered as the load for adhesive failure when coating rupture occurs and a fully exposed substrate is observed [54]. PHPS/LCS-RT is most resistant to cohesive failure as indicated by its high  $\rm L_{c1}$  value, and PHPS/LCS-200  $^{\circ}\text{C}$  has the highest  $\rm L_{c2}$ to resist adhesive failure. Meanwhile, the compressive stress generated during the scratch test induces noticeable buckles parallel to the scratch track [55]. We believe that the organic solvent in the PHPS/LCS-RT sample prevents the cohesive failure in the layer. With increasing pyrolysis temperature, the increased cohesive force due to crosslinking results in a brittle solid to decrease the cohesive strength. As a higher load is applied, part of the PHPS-derived coating is completely worn out and the substrate is exposed, as demonstrated in location 4 of Fig. 5(a-c).

The adhesion strength can be calculated from the following equation and the results are given in Table 3:

$$F = \frac{H}{\sqrt{\frac{H\pi R^2 - L_{c2}}{L_{c2}}}}$$
 (6)

where H is the hardness of the substrate ( $\sim 3170\,N/mm^2$ ), R is the tip radius, and  $L_{c2}$  is the critical load causing adhesive failure [56]. Table 3 shows that the adhesion strength is enhanced when the pyrolysis temperature increases from room temperature to 200 °C. However, when the pyrolysis temperature reaches 600 °C, the covalent Fe—O—

Si bonds are destructed to a certain extent, resulting in adhesion strength reduction. Hence, it is necessary to control the pyrolysis temperature in order to balance the covalent bond formation and destruction between the PHPS-derived coating and the substrate, ultimately obtaining high adhesion strength.

#### 3.3. Corrosion behaviors

Fig. 6(a) shows the typical potentiodynamic polarization (PD) curves of the PHPS/LCS-RT, PHPS/LCS-200 °C, and PHPS/LCS-600 °C samples in the 0.6 M NaCl solution, at the corrosion-only condition. Fig. 6(b) will be discussed in Section 3.4. In Fig. 6, it can be seen that both the anodic and cathodic polarization curves of the coated samples shift to much smaller current density values compared to that of bare steel, indicating significantly reduced corrosion kinetics due to the presence of the PHPS coating. In addition, Ecorr decreases with increasing pyrolysis temperature. The reduced  $E_{\text{corr}}$  indicates a slightly more active surface at a higher temperature. For a ceramic coating surface in an aqueous solution, corrosion involves complex processes including ion exchange between the electrolyte and coating, hydrolysis of network forming species (e.g., silica), and dissolution of hydrolyzed species into the electrolyte. In the current work, we believe the change in E<sub>corr</sub> is closely related to the coating microstructure, especially porosity and surface roughness. The PHPS in the current study is 20 wt% in dibutyl ether, and the evaporation of the solvent when using such a diluted system is more likely to cause pore formation although the pre-pyrolysis treatment used obviously decreases the overall number of pores. This small number of bubbles in the PHPS/LCS-600 °C sample is likely to cause the observed cathodic shift in E<sub>corr</sub>. However, the decrease of the surface roughness on the PHPS/LCS-600 °C sample makes E<sub>corr</sub> more positive. Pore formation and surface roughness both affect the value of E<sub>corr</sub>, but the former is to decrease Ecorr and the latter is to increase the  $E_{\text{corr}}$ . It is hard to differentiate which effect is dominant. This is why the PHPS-derived coating pyrolyzed at 600 °C has the most negative Ecorr value.

The surface morphologies of the coatings after the corrosion tests are shown in Fig. 7(a–c). Rough surfaces for PHPS/LCS-RT are observed due to the presence of uncrosslinked gel-like PHPS. With the temperature increase to 200 °C, the PHPS crosslinking decreases surface irregularity. After the 600 °C pyrolysis, the extensive formation of the Si—O—Si bonds results in a very smooth and compact surface (Fig. 7(c)), consistent with the results in Fig. 2(d–f). There is no observable corrosion in Fig. 7(a and b) while some blister defects are seen in Fig. 7(c). The latter may be caused by the diffusion of corrosive species and the related stress, along with the in-plane compressive stress in the coating due to temperature change [57].

Fig. 7(d–f) show the cross-sectional images of the PHPS/LCS-RT, PHPS/LCS-200 °C, and PHPS/LCS-600 °C samples after the corrosion tests. There is an apparent reduction in the coating thickness for PHPS/LCS-RT and PHPS/LCS-200 °C compared with that in Fig. 2(a–c), decreasing by 29 % and 30 %, respectively. However, no obvious thickness difference is observed for PHPS/LCS-600 °C, indicating a lower dissolution rate. Thus, the PHPS/LCS-600 °C coating should have better corrosion protection on the LCS substrate.

Corrosion resistance is dependent on many factors, such as microstructure, coating composition, surface roughness, and defect density [36]. For the PHPS-derived coatings, it can be understood from the following aspects. First, at low temperatures, an extensive amount of Si-H bonds still exists in the PHPS-derived coatings, as can be derived from Fig. 3. Second, the low crosslinking density of the PHPS coating allows Na<sup>+</sup> and Cl<sup>-</sup> diffusion towards the coating-substrate interface, resulting in higher corrosion rates for PHPS/LCS-RT and PHPS/LCS-200 °C, ultimately causing the coating thickness reduction [58,59]. Third, with the pyrolysis temperature increase to 600 °C, the

silanol groups undergo a self-condensation reaction to form Si—O—Si bonds along with the remaining Si—N bonds. This leads to a dense SiON structure and a passivating barrier layer to slow down the corrosion rate and coating thickness reduction [49]. Meanwhile, the hardness and Young's modulus both reach the maximum values for PHPS/LCS-600°C (Fig. 4) due to the formation of the dense SiON layer on the surface. With the surface roughness transition from rough to smooth with the temperature increase to 600°C, as shown in Fig. 2(a–c), active corrosive locations on the surface are reduced and the corrosion resistance is improved.

Blister defects can be observed on the PHPS/LCS-600 °C surface, likely due to the diffusion-induced stress from the corrosive species in the coating [57]. With the blister propagation and corrosive species diffusion, microcracks are induced, which may form a pathway through the coating barrier, reduce the adhesion between the coating and the substrate, and cause the coating to delaminate [60]. However, the thermal expansion of the polymeric coating during crosslinking is believed to be greater than the steel substrate, which should lead to compressive residual stress after the coating formation [61] and limit the pathways for the corrosive species to diffuse towards the interface [62]. Overall, PHPS/LCS-600 °C has the best corrosion protection on the LCS in the 0.6 M NaCl solution.

The EIS results are shown in Fig. 8, where the experimental data were fitted using an equivalent circuit (EC) model shown in Fig. 8(a). Table 4 summarizes all fitting parameters of the EC model. Such a model has been found to be quite successful for modeling coated metal systems [63]. In this EC model,  $R_{\Omega}$  is the electrolyte resistance,  $R_{\text{p}}$  represents the resistance of ion-conducting paths in the coating, and Cc is the capacitance of the intact coating. The coating and bare metal interface is modeled with R<sub>ct</sub> and a constant phase element (CPE) in parallel, where the former represents the charge-transfer resistance, and the later represents the non-ideal capacitive behavior of the double layer and diffusion processes. For the bare steel sample, due to the absence of a coating, the same EC model is used but the absence of  $C_{c}$  and  $R_{p}$  is assumed (i.e., resembling that of a simple Randles circuit). From Fig. 8(b-d), it can be seen that this selected model works well for fitting the experimental results of the Bode and Nyquist plots. The Bode plot shows a larger impedance modulus |Z| at the low-frequency limit for all PHPS coated LCS samples than that of bare LCS. Consistent with the PD results, this means that the PHPS coating is highly effective in mitigating corrosion for LCS. Fig. 8(c) shows that the phase angle of PHPS/LCS-600 °C remains close to 90° for most of the high frequency range covered in the measurements, indicating a good capacitive response and high corrosion resistance. It should be noticed that two well-separated semicircles are observed in the Nyquist plot of the PHPS/LCS-RT sample. The first semicircle is likely related to the properties of the PHPS-derived coating, and the second corresponds to the corrosion process happening at the substrate/coating interface [64]. In Fig. 8(d), the semicircle in the high frequency region of PHPS/LCS-600°C is larger than the corresponding semicircles of all other samples, indicating its highest corrosion resistance, in agreement with the PD test results. In Table 4, the EIS test fitting parameters show that both R<sub>p</sub> and R<sub>ct</sub> increase with the pyrolysis temperatures for the three coated samples. Uncoated LCS samples have the lowest  $R_{ct}$  of  $\sim 6.70 \times 10^{-2} \ \Omega \cdot cm^2$ . PHPS/LCS-600 °C exhibits the highest  $R_p$  and  $R_{ct}$ , which means that the coating after 600  $^{\circ}$ C pyrolysis possesses the highest resistance to the transfer of electrons across the metal surface. The impedance of the CPE is defined as

$$Z = \frac{1}{Y(j\omega)^n} \tag{7}$$

where Y is a constant, j is the imaginary unit,  $\omega$  is the angular frequency of the sinusoidal signal, and n is an exponent in the range of 0 < n < 1. The calculated values of CPE of all coated samples are

 $\sim \! 1.40 - \! 2.05 \times 10^{-5}$  F/cm², as listed in Table 4, which is similar to the double layer capacitance of  $\sim \! 10^5$  F/cm² in literature [65].

#### 3.4. Tribocorrosion behaviors

Fig. 6(b) shows the potentiodynamic polarization curves under 1 N constant load sliding in the 0.6 M NaCl solution. Compared to Fig. 6(a), sliding causes the corrosion potential and current density of the bare LCS to shift towards the right corner, suggesting the breakdown of the natural surface oxide layer of the bare LCS. Among all the samples, the electrochemical behaviors of the bare LCS are still the most active ones. Although the current density of the PHPS-derived coatings has a similar transformation as that of the bare LCS, i.e., the corrosion current density is increased by wear, their corrosion potential shifts to more positive values than that of the pure corrosion condition. At the anodic branch of PHPS/LCS-200 °C and PHPS/LCS-600 °C, an active-passive type of behavior is observed due to the effect of wear. However, the anodic behaviors of PHPS/LCS-RT seem to be similar to those of the bare LCS because part of the coating was removed by sliding. Fig. 9(c) shows that the mass loss of PHPS/LCS-600 °C is the least, indicting its best tribocorrosion resistance.

The variation of OCP of all specimens was recorded during the tribocorrosion tests as shown in Fig. 9(a). The dashed lines mark the start and end of the test. Before the indenter probes the surface, the OCP remains almost constant at their respective values. While this stationary status of all the specimens is broken and the potential drops after the load is applied (i.e., depassivation), the potential shift of PHPS/LCS-RT is the most extensive (~188.3 mV), followed by PHPS/LCS-200 °C (~88.7 mV) while the shift of PHPS/LCS-600°C was the least (~ 7 mV). Typically, the negative shift of OCP during tribocorrosion indicates that the surface layer is thermodynamically less stable with a weakened protective effect. Once the tribocorrosion test is finished, the potential of the samples is almost restored to their initial OCP values, indicating a repassivation of the worn area. Interestingly, the potential shift of bare LCS is only around 5.7 mV, even less than that of PHPS/LCS-600 °C. Indeed, the potential of active metals is not sensitive to sliding because of the lack of surface passivity [66], which is in good agreement with their electrochemical behaviors. Fig. 9(b) shows that the values of COF under OCP during tribocorrosion tests decrease in the order of PHPS/LCS-RT, PHPS/LCS-200 °C, and PHPS/LCS-600 °C, consistent with their mass loss tendency, as shown in Fig. 9(c).

To further assess the protection capability of the PHPS-derived coatings under simultaneous mechanical and chemical attacks. The friction force, COF, and current variation of the coated samples and bare LCS during the tribocorrosion test in the 0.6 M NaCl aqueous solution are shown in Fig. 10. The samples have been exposed to air under a linear ramping load at 0.4V anodic potential. The current for PHPS/ LCS-600 °C is ~2 orders lower than that of PHPS/LCS-RT and PHPS/ LCS-200 °C, and ~5 orders of magnitude lower than that of the bare LCS. At the beginning of the tests, the current shows almost no change. This means that the surface is still protective. Some COF spikes can be observed for all the samples, particularly for the bare LCS, due to the extremely low normal load since COF is derived from the friction force/ normal load [67]. As the load progressively increases, the friction force and COF linearly increase until a current increase is observed, suggesting coating failure. The normal load that causes the dramatic current increase is considered as the critical load. The failure time of PHPS/ LCS-RT and PHPS/LCS-200 °C is ~34 s and 36 s respectively, corresponding to the critical load of  $\sim 0.11 \, \mathrm{N}$  and  $\sim 0.12 \, \mathrm{N}$ , respectively. It is worth noting that there are two critical loads for PHPS/LCS-600°C. The first critical load of  ${\sim}0.05\,\mathrm{N}$  appears at  ${\sim}~15\,\mathrm{s},$  resulting in a slightly increased current. This current rise is caused by the blister defects on the surface, which has been demonstrated in Fig. 10(d). With the load increase, the actual coating failure occurs at ~ 52s, which corresponds

to the second critical load of  $\sim$ 0.17 N. At the end of the test, the current gradually shifts towards the original state because of surface passivation

The surface morphology of the wear tracks after tribocorrosion at different conditions and elemental (Si, O, N, and Fe) distributions at the failure locations under 0.4 V anodic potential are presented in Fig. 11. PHPS/LCS-RT and PHPS/LCS-200 °C show coating rupture failures and almost delamination. At all the conditions studied, the shedding area caused by the wear track obviously decreases with increasing pyrolysis temperature, indicating improved wear resistance at higher pyrolysis temperatures. Higher oxygen concentrations are shown on the exposed LCS substrates. Since there is no coating delamination in the first failure location for PHPS/LCS-600 °C, the oxygen concentration of the second failure location is shown and the value is  $27.02 \pm 0.34$  at.%, which is lower than that of PHPS/LCS-RT ( $58.86 \pm 1.96$  at.%) and PHPS/LCS-200 °C ( $59.33 \pm 1.84$  at.%), suggesting a lower corrosion rate for PHPS/LCS-600 °C [68]. The formation of a Si—O—Si network layer hinders oxygen diffusion.

From the electrochemical kinetics point of view, the coating should remain stable under an applied potential for corrosion protection. When an excessive load is applied, the protection may be destroyed, resulting in the current increase [66]. The critical loads for PHPS/LCS-RT and PHPS/LCS-200°C approach that for adhesion failure; and their failure time in the tribocorrosion test is earlier than that of the dry progressive scratch test. This means that PHPS/LCS-RT and PHPS/LCS-200°C fail due to corrosion-induced adhesion loss. At the same time, the hardness of PHPS/LCS-RT and PHPS/LCS-200°C is weakened under the corrosion attack. Several cracks over the failure locations provide corrosion pathways between the corrosive NaCl solution and the fresh LCS surface, resulting in the current increase. With regard to PHPS/LCS-600 °C, the first critical load should be ignored due to the extremely low current variation. The second critical load (~0.17 N), which induces the coating failure, is higher than that leading to the adhesion failure. The failure time is delayed to ~52 s. Thus, the PHPS/LCS-600 °C coating layer is most effective for corrosion protection. In addition, local coating defects and blisters can give rise to substrate dissolution through reaction with oxygen and further increase hydroxyl concentration outside the defects/ blisters, causing film delamination and blister growth [69]. At the surrounding of the failure location, obviously broken blisters with the exposed substrate can be seen in PHPS/LCS-600 °C.

#### 4. Conclusions

In this study, the pyrolysis temperature plays a significant role in the microstructure evolution and corrosion protection of the PHPS-derived coatings. The average surface roughness of the coating decreases while the hardness and Young's modulus increase with the pyrolysis temperature, due to the formation of Si—O—Si bonds. The PHPS-derived coating acts as an effective layer on LCS in a chlorine environment, especially for the sample pyrolyzed at 600 °C. The corrosion kinetics of coated LCS is significantly reduced compared to that of the bare LCS. The protection efficiency of the PHPS/LCS-600 °C coating is better than that of the PHPS/LCS-RT and PHPS/LCS-200 °C coatings. The PHPS-derived coatings have a significant effect on the tribocorrosion resistance improvement of low carbon steel. PHPS/LCS-600 °C has the best performance due to its the highest hardness and best corrosion resistance. The PHPS-derived coatings can be used for corrosion protection of metals in automotive industry, coastal infrastructure, naval systems, among others.

#### Data availability

The raw data required to reproduce these findings are available to download from https://data.lib.vt.edu/.

CRediT authorship contribution statement

Ni Yang: Conceptualization, Resources, Data curation, Formal analysis, Investigation, Methodology, Validation, Visualization, Software, Writing - original draft, Writing - review & editing. Wenbo Wang: Conceptualization, Resources, Data curation, Formal analysis, Investigation, Methodology, Validation, Visualization, Software, Writing - original draft, Writing - review & editing. Wenjun Cai: Conceptualization, Formal analysis, Funding acquisition, Investigation, Methodology, Project administration, Resources, Software, Supervision, Validation, Writing - original draft, Writing - review & editing. Kathy Lu: Conceptualization, Formal analysis, Funding acquisition, Investigation, Methodology, Project administration, Resources, Software, Supervision, Validation, Writing - original draft, Writing - review & editing.

#### **Declaration of Competing Interest**

None.

#### Acknowledgments

This work was supported by the US National Science Foundation under grant numbers CMMI-1634325 and CMMI-1855651.

#### Appendix A. Supplementary data

Supplementary material related to this article can be found, in the online version, at doi:https://doi.org/10.1016/j.corsci.2020.108946.

#### References

- Y.S. Choi, J.J. Shim, J.G. Kim, Effects of Cr, Cu, Ni and Ca on the corrosion behavior of low carbon steel in synthetic tap water, J. Alloys. Compd. 391 (2005) 162–169.
- [2] V.L. Finkenstadt, G.L. Côté, J. Willett, Corrosion protection of low-carbon steel using exopolysaccharide coatings from Leuconostoc mesenteroides, Biotechnol. Lett. 33 (2011) 1093–1100.
- [3] B. Pollard, Spot welding characteristics of HSLA steel for automotive applications, Weld. J. 53 (1974) 343.
- [4] W. Bendick, J. Gabrel, B. Hahn, B. Vandenberghe, New low alloy heat resistant ferritic steels T/P23 and T/P24 for power plant application, Int. J. Pressure Vessels Piping. 84 (2007) 13–20.
- [5] D.V. Edmonds, R.C. Cochrane, The effect of alloying on the resistance of carbon steel for oilfield applications to CO<sub>2</sub> corrosion, Mater. Res. 8 (2005) 377–385.
- [6] W. Garrison, Ultrahigh-strength steels for aerospace applications, JOM. 42 (1990) 20–24
- [7] J.O. Iroh, W. Su, Corrosion performance of polypyrrole coating applied to low carbon steel by an electrochemical process, Electrochim. Acta46 (2000) 15–24.
- [8] P. Seré, M. Zapponi, C. Elsner, A. Di Sarli, Comparative corrosion behaviour of 55Aluminium-zinc alloy and zinc hot-dip coatings deposited on low carbon steel substrates, Corros. Sci. 40 (1998) 1711–1723.
- [9] C.Y. Bai, M.D. Ger, M.S. Wu, Corrosion behaviors and contact resistances of the low-carbon steel bipolar plate with a chromized coating containing carbides and nitrides, Int. J. Hydrogen Energy34 (2009) 6778–6789.
- [10] J. Jiang, Y. Wang, Q. Zhong, Q. Zhou, L. Zhang, Preparation of Fe<sub>2</sub>B boride coating on low-carbon steel surfaces and its evaluation of hardness and corrosion resistance, Surf. Coat. Technol. 206 (2011) 473–478.
- [11] V. Shinde, S.R. Sainkar, S.A. Gangal, P.P. Patil, Synthesis of corrosion inhibitive poly(2,5-dimethylaniline) coatings on low carbon steelJ. Mater. Sci. 41 (2006) 2851–2858.
- [12] A. Sheibani Aghdam, S.R. Allahkaram, S. Mahdavi, Corrosion and tribological behavior of Ni–Cr alloy coatings electrodeposited on low carbon steel in Cr (III)–Ni (II) bath, Surf. Coat. Technol. 281 (2015) 144–149.
- [13] R.M. Bandeira, J. van Drunen, G. Tremiliosi-Filho, J.R. dos Santos, J.M.E. de Matos, Polyaniline/polyvinyl chloride blended coatings for the corrosion protection of carbon steel, Prog. Org. Coat. 106 (2017) 50–59.
- [14] V. Shinde, S. Sainkar, P. Patil, Electrochemical synthesis and corrosion protection properties of poly (o-toluidine) coatings on low carbon steel, J. Appl. Polym. Sci. 96 (2005) 685–695.
- [15] H.P. Hack, Galvanic Corrosion, ASTM International, 1988.

[16] G. Zheng, C. Wang, A. Pei, J. Lopez, F. Shi, Z. Chen, A.D. Sendek, H.-W. Lee, Z. Lu, H. Schneider, High-performance lithium metal negative electrode with a soft and flowable polymer coating, ACS Energy Lett. 1 (2016) 1247–1255.

- [17] M. Günthner, T. Kraus, A. Dierdorf, D. Decker, W. Krenkel, G. Motz, Advanced coatings on the basis of Si (C) N precursors for protection of steel against oxidation, J. Eur. Ceram. Soc. 29 (2009) 2061–2068.
- [18] G. Wen, F. Li, L. Song, Structural characterization and mechanical properties of Si-BONC ceramics derived from polymeric precursors, Mater. Sci. Eng. A. 432 (2006) 40–46.
- [19] J. Xu, J. Favergeon, P. Mazeran, G. Moulin, C. Vu, Use of silicon-based coating for high temperature protection of metallic alloys, Mater. Sci. Forum. 696 (2011) 308–313
- [20] M. Parchovianský, I. Petrikova, G. Barroso, P. Švančárek, D. Galuskova, G. Motz, D. Galusek, Corrosion and oxidation behavior of polymer derived ceramic coatings with passive glass fillers on AISI 441 stainless steel, Ceram.—Silikáty. 62 (2018) 146–157.
- [21] J.D. Torrey, R.K. Bordia, Mechanical properties of polymer-derived ceramic composite coatings on steel, J. Eur. Ceram. Soc. 28 (2008) 253–257.
- [22] M. Parchovianský, G. Barroso, I. Petríková, G. Motz, D. Galusková, D. Galusek, Polymer derived glass ceramic layers for corrosion protection of metals, Adv. Refrac. Ceram. Energ. Conserv. Effic. 256 (2016) 187–200.
- [23] K. Mohite, Y. Khollam, A. Mandale, K. Patil, M. Takwale, Characterization of silicon oxynitride thin films deposited by electron beam physical vapor deposition technique, Mater. Lett. 57 (2003) 4170–4175.
- [24] N. Shibata, Plasma-chemical vapor-deposited silicon oxide/silicon oxynitride double-layer antireflective coating for solar cells, J. Appl. Phys. 30 (1991) 997.
- [25] K. Watanabe, M. Sakairi, H. Takahashi, K. Takahiro, S. Nagata, S. Hirai, Anodizing of aluminum coated with silicon oxide by a sol-gel method, J. Electrochem. Soc. 148 (2001) B473\_B481
- [26] P. Martin, A. Bendavid, J. Cairney, M. Hoffman, Nanocomposite Ti–Si–N, Zr–Si–N, Ti–Al–Si–N, Ti–Al–V–Si–N thin film coatings deposited by vacuum arc deposition, Surf. Coat. Technol. 200 (2005) 2228–2235.
- [27] M. Morks, Fabrication and characterization of plasma-sprayed  $\rm HA/SiO_2$  coatings for biomedical application, J. Mech. Behav. Biomed. Mater. 1 (2008) 105–111.
- [28] Y. Wang, W. Fei, L. An, Oxidation/corrosion of polymer-derived SiAlCN ceramics in water vapor, J. Am. Ceram. Soc. 89 (2006) 1079–1082.
- [29] K. Bawane, K. Lu, Q. Li, R. Bordia, High temperature oxidation behaviors of SiON coated AISI 441 in Ar + O<sub>2</sub>, Ar + H<sub>2</sub>O, and Ar + CO<sub>2</sub> atmospheres, Corros. Sci. 166 (2020), 108429.
- [30] J.D. Torrey, R.K. Bordia, Phase and microstructural evolution in polymer-derived composite systems and coatings, J. Mater. Res. 22 (2007) 1959–1966.
- [31] S. Bernard, P. Miele, Polymer-derived boron nitride: a review on the chemistry, shaping and ceramic conversion of borazine derivatives, Mater. 7 (2014) 7436–7459.
- [32] O. Funayama, Y. Tashiro, A. Kamo, M. Okumura, T. Isoda, Conversion mechanism of perhydropolysilazane into silicon nitride-based ceramics, J. Mater. Sci. 29 (1994) 4883–4888.
- [33] O. Funayama, T. Aoki, T. Kato, M. Okoda, T. Isoda, Synthesis of thermosetting copolymer of polycarbosilane and perhydropolysilazane, J. Mater. Sci. 31 (1996) 6369–6375.
- [34] Z. Zhang, Z. Shao, Y. Luo, P. An, M. Zhang, C. Xu, Hydrophobic, transparent and hard silicon oxynitride coating from perhydropolysilazane, Polym. Int. 64 (2015) 971–978.
- [35] K. Wang, X. Zheng, F.S. Ohuchi, R.K. Bordia, The conversion of perhydropolysilazane into SiON films characterized by X-ray photoelectron spectroscopy, J. Am. Ceram. Soc. 95 (2012) 3722–3725.
- [36] R. Bertoncello, A. Vezzoli, E. Rebollo, Corrosion behaviour of room temperature cured polysilazane-derived silica coatings on Al 5086, Int. J. Eng. Res. Sci. Technol. 2 (2016) 105–112.
- [37] F. Riffard, E. Joannet, H. Buscail, R. Rolland, S. Perrier, Beneficial effect of a pre-ceramic polymer coating on the protection at 900 °C of a commercial AISI 304 stainless steel, Oxid. Met. 88 (2017) 211–220.
- [38] K. Wang, M. Günthner, Gn. Motz, B.D. Flinn, R.K. Bordia, Control of surface energy of silicon oxynitride films, Langmuir 29 (2013) 2889–2896.
- [39] Y. Iwase, Y. Horie, Y. Daiko, S. Honda, Y. Iwamoto, Synthesis of a novel polyethoxysilsesquiazane and thermal conversion into ternary silicon oxynitride ceramics with enhanced thermal stability, Materials 10 (2017) 1391.
- [40] L. Blankenburg, M. Schrödner, Perhydropolysilazane derived silica for flexible transparent barrier foils using a reel-to-reel wet coating technique: single-and multilayer structures, Surf. Coat. Technol. 275 (2015) 193–206.
- [41] W.C. Oliver, G.M. Pharr, An improved technique for determining hardness and elastic modulus using load and displacement sensing indentation experiments, J. Mater. Res. 7 (1992) 1564–1583.
- [42] S. Acharya, A.G. Panicker, V. Gopal, S.S. Dabas, G. Manivasagam, S. Suwas, K. Chatterjee, Surface mechanical attrition treatment of low modulus Ti-Nb-Ta-O alloy for orthopedic applications, Mater. Sci. Eng. C 110 (2020), 110729.

- [43] M. Monti, B. Dal Bianco, R. Bertoncello, S. Voltolina, New protective coatings for ancient glass: silica thin-films from perhydropolysilazane, J. Cult. Herit. 9 (2008) 143–145
- [44] M. Günthner, K. Wang, R.K. Bordia, G. Motz, Conversion behaviour and resulting mechanical properties of polysilazane-based coatings, J. Eur. Ceram. Soc. 32 (2012) 1883–1892.
- [45] I.S. Chuang, G.E. Maciel, A detailed model of local structure and silanol hydrogen bonding of silica gel surfaces, J. Phys. Chem. B 101 (1997) 3052–3064.
- [46] L. Hu, et al., Perhydropolysilazane derived silica coating protecting Kapton from atomic oxygen attack, Thin Solid Films 520 (2011) 1063–1068.
- [47] A. Schutz, M. Gunthner, G. Motz, O. Greissl, U. Glatzel, Characterisation of novel precursor-derived ceramic coatings with glass filler particles on steel substrates, Surf. Coat. Tech. 207 (2012) 319–327.
- [48] G.M. Choi, et al., Flexible hard coating: glass-like wear resistant, yet plastic-like compliant, transparent protective coating for foldable displays, Adv. Mater. 29 (2017), 1700205.
- [49] M. Günthner, T. Kraus, W. Krenkel, G. Motz, A. Dierdorf, D. Decker, Particle-filled PHPS silazane-based coatings on steel, Int. J. Appl. Ceram. Technol. 6 (2009) 373–380
- [50] R. Saito, Si. Kobayashi, H. Hayashi, T. Shimo, Surface hardness and transparency of poly (methyl methacrylate)-silica coat film derived from perhydropolysilazane, J. Appl. Polym. Sci. 104 (2007) 3388–3395.
- [51] F. Bauer, U. Decker, A. Dierdorf, H. Ernst, R. Heller, H. Liebe, R. Mehnert, Preparation of moisture curable polysilazane coatings: part I. Elucidation of low temperature curing kinetics by FT-IR spectroscopy, Prog. Org. Coat. 53 (2005) 183–190.
- [52] L. Storozhuk, N. Iukhymenko, Iron oxide nanoparticles modified with silanes for hyperthermia applications, Appl. Nanosci. 9 (2019) 889–898.
- [53] E. Rabkin, B. Straumal, V. Semenov, W. Gust, B. Predel, The influence of an ordering transition on the interdiffusion in Fe-Si alloys, Acta Metall. Mater. 43 (1995) 3075–3083.
- [54] A.A.A. Aliyu, A.M. Abdul-Rani, T.V.V.L.N. Rao, E. Axinte, S. Hastuty, R.P. Parameswari, J.R. Subramaniam, S.P. Thyagarajan, Characterization, adhesion strength and in-vitro cytotoxicity investigation of hydroxyapatite coating synthesized on Zr-based BMG by electro discharge process, Surf. Coat. Technol. 370 (2019) 213–226.
- [55] A. Kleinbichler, M. Pfeifenberger, J. Zechner, S. Wöhlert, M. Cordill, Scratch induced thin film buckling for quantitative adhesion measurements, Mater. Des. 155 (2018) 203–211.
- [56] A. Schütz, M. Günthner, G. Motz, O. Greil, U. Glatzel, Characterisation of novel precursor-derived ceramic coatings with glass filler particles on steel substrates, Surf. Coat. Technol. 207 (2012) 319–327.
- [57] M. Nazir, Z.A. Khan, A. Saeed, K. Stokes, A model for cathodic blister growth in coating degradation using mesomechanics approach, Mater. Corros. 67 (2016) 495–503.
- [58] R. Suleiman, H. Dafalla, B. El Ali, Novel hybrid epoxy silicone materials as efficient anticorrosive coatings for mild steel, RSC Adv. 5 (2015) 39155–39167.
- [59] J.D. Torrey, R.K. Bordia, Processing of polymer-derived ceramic composite coatings on steel, J. Am. Ceram. Soc. 91 (2008) 41–45.
- [60] K. Holmberg, A. Mathews, Coatings tribology: a concept, critical aspects and future directions, Thin Solid Films253 (1994) 173–178.
- [61] F.Z. Xuan, S.S. Shao, Z. Wang, S.-T. Tu, Influence of residual stress on diffusion-in-duced bending in bilayered microcantilever sensors, Thin Solid Films518 (2010) 4345–4350
- [62] M.H. Nazir, Z.A. Khan, K. Stokes, Analysing the coupled effects of compressive and diffusion induced stresses on the nucleation and propagation of circular coating blisters in the presence of micro-cracks, Eng. Failure Anal. 70 (2016) 1–15.
- [63] B.V. Jegdić, et al., The EIS investigation of powder polyester coatings on phosphated low carbon steel: the effect of  ${\rm NaNO_2}$  in the phosphating bath, Corros. Sci. 53 (2011) 2872–2880.
- [64] R.M. Souto, et al., Comparative EIS study of different Zn-based intermediate metallic layers in coil-coated steels. Corros. Sci. 48 (2006) 1182–1192.
- [65] S.L. Wu, Z.D. Cui, G.X. Zhao, M.L. Yan, S.L. Zhu, X.J. Yang, EIS study of the surface film on the surface of carbon steel from supercritical carbon dioxide corrosion, Appl. Surf. Sci. 228 (2004) 17–25.
- [66] S. Mischler, Triboelectrochemical techniques and interpretation methods in tribocorrosion: a comparative evaluation, Tribol. Int. 48 (2008) 573–583.
- [67] C.N. Cai, C. Zhang, Y.S. Sun, H.-H. Huang, C. Yang, L. Liu, ZrCuFeAlAg thin film metallic glass for potential dental applications, Intermetallics86 (2017) 80–87.
- [68] G. Cox, B. Roetheli, Effect of oxygen concentration on corrosion rates of steel and composition of corrosion products formed in oxygenated water, Ind. Eng. Chem. 23 (1931) 1012–1016.
- [69] P. Seré, et al., The surface condition effect on adhesion and corrosion resistance of carbon steel/chlorinated rubber/artificial sea water systems, Corros. Sci. 38 (1996) 853–866.